The DOI for this manuscript is doi: 10.1175/JCLI-D-17-0574.1

The final published version of this manuscript will replace the preliminary version at the above DOI once it is available.

If you would like to cite this EOR in a separate work, please use the following full citation:

Ting, M., R. Seager, C. Li, H. Liu, and N. Henderson, 2018: Mechanism of Future Spring Drying in the Southwest U.S. in CMIP5 Models*. J. Climate. doi:10.1175/JCLI-D-17-0574.1, in press.

Mechanism of Future Spring Drying in the Southwest U.S. in CMIP5 Models*

Mingfang Ting, Richard Seager, Cuihua Li, Haibo Liu and Naomi Henderson
Lamont-Doherty Earth Observatory
Columbia University

Submitted to *Journal of Climate*
August 24, 2017,
Revised December 18th, 2017

Corresponding author address: Mingfang Ting, Lamont-Doherty Earth Observatory
Columbia University
E-mail: ting@ldeo.columbia.edu
*LDEO Contribution Number : xxxx

ABSTRACT

The net surface water budget, precipitation minus evaporation (P-E), shows a clear seasonal cycle in the American Southwest with net gain of surface water (positive P-E) in the cold half of the year (October to March) and net loss of water (negative P-E) in the warm half (April – September), with June and July being the driest months of the year. There is a significant shift of the summer drying toward earlier in the year under a CO_2 warming scenario, resulting in substantial spring drying (MAM) of the American Southwest, from the near-term future to the end of the current Century with gradually increasing magnitude. While the spring drying has been identified in previous studies, its mechanism has not been fully addressed. Using moisture budget analysis, we found that the drying is mainly due to decreased mean moisture convergence, partially compensated by the increase in transient eddy moisture flux convergence. The decreased mean moisture convergence is further separated into components due to changes in circulation (dynamic changes) and changes in atmospheric moisture content (thermodynamic changes). The drying is found to be dominated by the thermodynamic driven changes in column averaged moisture convergence, due mainly to increased dry zonal advection caused by the climatological land-ocean thermal contrast, rather than by the well-known "dry get drier" mechanism. Furthermore, the enhanced dry advection in the warming climate is dominated by the robust zonal mean atmospheric warming, leading to equally robust spring drying in Southwest US.

1. Introduction

There is some agreement in previous studies that the Southwest United States (SWUS), a region stretching from the Southern Plains to the Pacific coast between 25 and 45N latitudes, will likely become drier in the greenhouse warming future (e.g., Seager et al., 2007, 2013; Seager and Vecchi, 2010; Scheff and Frierson, 2012). While these model-based projections echo the recent severe droughts in the Southwest, there is uncertainty as to the relative roles of radiative forcing and natural variability in driving recent precipitation history, although the latter appears dominant (e.g., Seager et al. 2015, Delworth et al. 2015, Prein et al., 2016). By comparison, there is widespread confidence that warming of the southwest, which creates a tendency to reduce soil moisture and streamflow, is ongoing and driven by climate change (e.g. Williams et al. 2015; Cook et al., 2014; 2015; Diffenbaugh et al., 2015). Given the growing demands for water in the region due to increasing population and economic growth, water resource management is expected to become increasingly challenging if recent trends continue and/or model projections are correct.

The future change in surface water availability is season dependent, as most of these areas have a net gain of surface water (precipitation minus evaporation, P - E) in the cold half of the year (October to March), and a net loss of water in the warm half (April – September) (Seager et al., 2014). Any seasonal shift of this pattern will add to the complexity of the water resource challenges. In addition, increasing surface temperature due to greenhouse warming will likely reduce snow pack and cause early melting, thus reducing the natural storage of surface water for summer usage (e.g., Mote, 2006; Pierce et al., 2008; Luce et al., 2014).

Seager et al. (2014) provided a detailed account of present day and near-term future changes in the hydrological cycle over North America using the moisture budget approach by separating into the warm and cold seasons using the European Centre for Medium Range Weather Forecasts ERA-Interim Reanalysis (ERA-I, Dee et al., 2011) and CMIP5 models' historical and future scenario (Representative Path Way 8.5, RCP85) simulations (Taylor et al., 2012). They found that during the winter half year, the models project drying of the Southwest due mainly to the reduction in mean moisture convergence. However, the exact mechanisms and the full seasonal cycle of the Southwest drying trend as projected in the model were not examined, nor whether this trend amplifies over time. Using a finer resolution regional climate model, Gao et al. (2014) examined seasonal changes of P – E for the end of the 21^{st} Century as compared to the present climate and found a robust spring drying in the southwestern U.S.. However, the physical mechanisms for this pronounced spring drying were also not clearly identified.

Unlike over the oceans, where changes in P – E are dominated by the so-called wet-get-wetter and dry-get-drier mechanism (e.g. Held and Soden, 2006) as a consequence of increasing atmospheric water vapor content in a warming climate, the continental hydroclimate change is more complex. For example, Boos (2012) and Byrne & O'Gorman (2015) found that changes in zonal temperature gradient, thus the associated atmospheric water vapor gradient, can be an important factor in P - E changes in the last glacial maximum and future warming climate, respectively. These studies, however, do not address specifically the SWUS region, or factors influencing the seasonal cycle of the P – E changes.

These previous studies led us to examine the multimodel CMIP5 future projections of the surface water balance and their seasonal change over the southwest in this study, focusing on the mechanisms of the changes and the development over time from the near future (2021-2040) to the end of the 21st Century. The rest of the paper is organized as follows. Section 2 presents the data and methods used in this study, followed by a discussion of the mechanisms for the climatological seasonal cycle of moisture budget in the Southwest U.S. in section 3. Section 4 provides the detailed mechanisms of the change in seasonal moisture budget and the spring drying, followed by a summary in section 5.

2. Data and Methods

We used the same 22 CMIP5 models (table 1) as in Seager et al. (2014) that have the available 6-hourly data for calculating transient eddy moisture fluxes necessary for the moisture budget analysis. These 22 models provide historical simulations with both anthropogenic and natural radiative forcings for the historical period and future projections with RCP8.5. In this study, we focus on the period 1979-2005 as the present-day base period, and the future changes (from 2021 to 2100) in hydroclimate and moisture budget are with respect to that reference period. In order to validate the present day CMIP5 simulations, we used the ERA-I Reanalysis (Dee et al, 2011) for the same period, 1979 – 2005, for direct comparisons.

Moisture budget analyses were performed for both the ERA-I and CMIP5 present and future simulations as in Seager and Henderson (2013). Briefly, the column-integrated moisture budget for a steady state atmosphere can be expressed in pressure coordinates as follows:

$$P - E = -\frac{1}{g\rho_w} \nabla \cdot \int_0^{p_s} \vec{u}\, q \mathrm{dp} \qquad (1)$$

where P represents precipitation, E evaporation/evapotranspiration, g is the gravitational constant, ρ_w is water density, p is pressure and p_s its surface value, q is specific humidity and $\vec{u}$ the horizontal wind vector. When averaging over a month, the column-integrated total moisture convergence (right side of Eq. 1) can be expressed as the sum of the monthly mean moisture convergence plus the sub-monthly transient eddy moisture convergence, as follows:

$$\bar{P} - \bar{E} = -\frac{1}{g\rho_w} \nabla \cdot \int_0^{p_s} \bar{\vec{u}}\, \bar{q} dp - \frac{1}{g\rho_w} \nabla \cdot \int_0^{p_s} \overline{\vec{u}' q'}\, dp \qquad (2)$$

where bar represents monthly mean and prime daily deviation from the monthly mean. The first term on the right-hand side of Eq. (2) can be further separated into three terms, relating to mean moisture advection and mass divergence as well as a boundary term as follows:

$$\nabla \cdot \int_0^{p_s} \bar{\vec{u}}\, \bar{q} dp = \int_0^{p_s} \bar{\vec{u}} \cdot \nabla \bar{q} dp + \int_0^{p_s} \bar{q}\, \nabla \cdot \bar{\vec{u}} dp + \bar{q}_s \overline{\vec{u}_s} \cdot \nabla p_s \qquad (3)$$

where $\bar{q}_s$ and $\overline{\vec{u}_s}$ represent the surface specific humidity and vector horizontal wind, respectively. The boundary term arises from the surface pressure gradient and can be large around mountains and represents in some sense moisture convergence and divergence at the surface due to the topography.

When the changes of the moisture budget are needed for two selected periods, we use δ to represent that change and Eq. (2) can be rewritten as follows:

$$\delta(\overline{\bar{P} - \bar{E}}) = \delta\left(\overline{-\frac{1}{g\rho_w} \nabla \cdot \int_0^{p_s} \bar{\vec{u}}\, \bar{q} dp}\right) + \delta\left(\overline{-\frac{1}{g\rho_w} \nabla \cdot \int_0^{p_s} \overline{\vec{u}' q'}\, dp}\right) \qquad (4)$$

where δ represents the difference between the two periods, and the long bar represents the period average. The first term on the right side of Eq. (4) can be further separated into terms representing changes in mean moisture convergence due to only changes in horizontal wind (dynamic, DYN) and that due to only changes in specific humidity (thermodynamic, TH) as follows:

$$\delta\left(\overline{-\frac{1}{g\rho_w}\nabla\cdot\int_0^{p_s}\bar{\bar{\vec{u}}}\,\bar{q}\,dp}\right) \cong \frac{1}{g\rho_w}\overline{\nabla\cdot\int_0^{p_s}\delta\bar{\bar{\vec{u}}}\,\overline{q_p}\,dp} + \frac{1}{g\rho_w}\overline{\nabla\cdot\int_0^{p_s}\left(\overline{\overline{\vec{u}_p}}\right)\delta\bar{q}\,dp}$$

$$= \delta\overline{\overline{DYN}} + \delta\overline{\overline{TH}} \qquad (5)$$

where $\delta\bar{\bar{\vec{u}}}=\overline{\overline{\vec{u}_f}} - \overline{\overline{\vec{u}_p}}$ and $\delta\bar{q} = \overline{q_f} - \overline{q_p}$, and subscript p represents past (1979-2005) monthly mean value and subscript f represent future monthly mean value. Note that the higher order nonlinear term involving the change in circulation and change in humidity is found to be negligible and not included in Eq. 5. These various decompositions will be used in the following to disentangle the role of the various physical processes in contributing to changes in future hydroclimate.

3. Climatological Seasonal Cycle of Moisture Budget in Southwest United States

While Seager et al. (2014) investigated many aspects of the North American moisture budget and their future changes in the winter and summer half years, they did not address the detailed seasonal cycle of the moisture budget and its change, particularly with respect to the semi-arid Southwest US (SWUS) region. Changes in seasonal cycle have important implications as water managers need to adjust to the changes when planning for water allocations throughout the year. Figure 1 shows the three-month mean seasonal (DJF, MAM, JJA, and SON) net surface water balance (P-E) using the ERA-I Reanalysis and CMIP5 multimodel mean (MMM). For the SWUS (depicted by the box), during winter (DJF) there is net gain of surface water over most of the domain except the southernmost region. For both spring (MAM) and summer (JJA), the SWUS is dominated by net loss of surface water, with stronger drying in the summer. The exception is the North American Monsoon region of surface water gain in summer in the southwest of the domain. By the fall, the drying of the SWUS lessens and turns into net surface wetting in the northern portion. This seasonal cycle is well reproduced by the CMIP5 MMM, except that the climatological spring drying is limited to the southern half of the domain, thus indicating a delay in the seasonal cycle of warm season drying. There is also a net gain of water in the fall season in models across the region, indicating a bias toward generally wetter conditions in the model climatology throughout the year.

To better illustrate how P-E changes throughout the season and to understand the mechanisms of the spring and summer drying, Fig. 2 shows the SWUS area average (box shown in Fig. 1) P-E along with the mean and transient moisture flux convergences (top three rows) and the mean moisture advection (fourth row) and mass divergence (fifth row) contributions to the total mean moisture convergence terms, along with the boundary term (sixth row), for both ERA-I Reanalysis and CMIP5 MMM, as a function of month. In the ERA-I Reanalysis, there is a net gain of surface water in the winter half year, from October to March, and net loss of water in the summer half year, from April to September. The peak drying time is in June and peak wet months are in December and January. The positive P-E during the winter half year is mainly due to synoptic storms converging moisture into the region, as indicated by the transient moisture convergence term (third row). The transient moisture flux convergence is offset by the mean moisture divergence out of the region (second row) which is negative throughout the year except in July and August when it is weakly positive. The climatological drying in the warmer half year is caused by mean moisture divergence in spring and transient moisture divergence in summer.

Furthermore, the mean moisture divergence is due to both mean mass divergence and moisture advection with the latter dominant. The mean moisture advection term is drying for the majority of the annual cycle and peaks in the late spring/early summer months. In this region of complex topography, the boundary term (sixth row) can be a large wetting factor peaking in summer that offsets the advective drying.

The CMIP5 MMM well represents the moisture budget terms and their seasonal cycle in the SWUS region. As shown in Fig. 1, the net surface water budget tends to have a wet bias in the region, causing a wetter winter and slightly less dry summer compared to ERA-I. The wet bias is mainly due to the transient eddy moisture flux convergence being too large (compare Fig. 2f to Fig. 2e). Other than these small discrepancies, the CMIP5 MMM reproduces well the main features of the moisture budget seasonal cycle and thus can be used for understanding the future changes in SWUS hydroclimate.

The dominant climatological drying contribution from the mean moisture advection (Figs. 2g, h) during the spring and summer is somewhat counterintuitive as one would expect prevailing westerlies in the region to bring moisture from the Pacific Ocean into the SWUS region to its east. Since the mean moisture advection turns out to be the dominant mechanism for the future spring drying as well, it is worthwhile to first explore the physical causes of its climatology. After examination, it turns out that the drying is due mainly to the zonal advection term (the meridional advection is secondary and of opposite sign). Thus, we focus below on the zonal moisture advection term.

Figure 3 shows the pressure-longitude vertical cross sections of specific humidity, air temperature, and zonal wind vectors averaged over the latitude span of 32-45N for the four seasons using ERA-I (left) and CMIP5 MMM (right). Since the zonal mean components of q and T do not contribute to the zonal advection, we only show their zonally asymmetric parts in Fig. 3. The specific humidity shows a relatively small east-west gradient during winter but a very strong zonal dipole structure in the summer with smaller q over the coastal region and larger q on top of the mountains and east of the Rockies. Both spring and autumn seasons show similar specific humidity structure as the summer but with smaller peaks over the highlands. The air temperature is influenced by the local topography and land sea contrasts with cooler temperature over the oceans and warmer temperature over land, particularly above the mountains in the summer. Part of the specific humidity zonal dipole can be explained by the zonally asymmetric temperature structure according to the Clausius-Clapeyron equation with uniform relative humidity at each level (not shown), and is thus driven by land-sea thermal contrasts and local topography. However, the zonally asymmetric q and T do not coincide with each other completely, suggesting that there are dynamical processes involved in shaping the q structure.

To further understand the climatological zonally asymmetric q structure in the region, we show in Fig. 4 the vertically integrated mean moisture transport for all four seasons based on both ERA-I and CMIP5 MMM, along with the 850 hPa specific humidity. In the winter, the moisture transport along the west coast is dominated by westerlies bringing relatively warm and humid air to the region in both reanalysis and CMIP5 MMM (top row). But from spring to fall, the mean moisture transport is dominated by the along-coast cool and dry advection from the north associated with the Pacific subtropical anticyclone while, further inland, it is dominated by the warm moist air from the Gulf of Mexico associated with the Great Plains Low Level Jet (LLJ, Ting and Wang, 2004, Jiang et al. 2007, Parish and Oolman 2010). These processes create a moisture gradient in the region that is dry over the coastal regions and moist further inland. Any zonal advection of moisture in the region would lead to advective drying from March to October (Figs. 2g, h).

The CMIP5 MMM shows very similar features of the zonally asymmetric q and T (right panels of Fig. 3), as well as the moisture transports (right panels of Fig. 4). with the strongest drying due to mean moisture advection occurring in June (Fig. 2h), slightly shifted compared to reanalysis observations. The results here suggest that the mean flow moisture divergence in the SWUS, which dominates the climatological warm season drying in the region, is mainly driven by the zonally asymmetric specific humidity gradients. The specific humidity gradients are a result of land-ocean thermal contrasts, local topography, as well as moisture transport associated with the Pacific subtropical anticyclone and the Great Plains low level jet. The next section examines how the zonal specific humidity gradient and the SWUS drying evolve in the future.

4. Changes in Seasonal Cycle of Moisture Budget and the Mechanisms of Spring Drying

The future changes in SWUS hydroclimate are explored by examining the four 20-year future periods, starting from 2021-2040 to 2081 -2100. Figure 5a illustrates changes in net surface water balance, P – E, from each of the 20-year periods with respect to the recent period, 1979 – 2005. These maps show the general drying trend in the SWUS region throughout the seasonal cycle except January and February when the changes are slightly positive for all future periods. More notable is that the spring season, MAM, consistently shows the strongest drying signal, effectively shifting forward the peak drying season of negative P-E from mid-summer (top row in Fig. 2) towards late spring/early summer (see Fig. 10). The amplitude of the drying also increases steadily from the near-term future to the end of the 21st Century. When separating the future drying into the mean and transient contributions in Fig. 5, it is clear that spring drying is predominantly caused by the mean moisture divergence (Fig. 5b), whereas in the summer, drying by transient eddy moisture divergence (Fig. 5c) is largely cancelled by mean flow wetting leading to little change in P-E. Given the large amplitude of the spring drying, we focus the rest of the paper on the mechanisms responsible.

Figure 6 shows the spatial patterns of the spring drying for the four periods in terms of P-E. The spatial pattern of the drying is robustly similar across the four periods with increasing amplitude toward the future and it is particularly strong in the northern part of the domain, from the California coast to Colorado. In the southern tip of the domain, there is actually a slight wetting trend. To gain further insights into the spring drying mechanisms, we show in Fig. 7 the area-averaged moisture budget changes for the four future periods with respect to the recent period, for P-E, total mean moisture convergence and transient moisture flux convergence (Fig. 7a-c). Consistent with Figs. 5 and 6, there is a dominant spring drying in terms of P-E, and this drying is entirely due to the mean moisture divergence, offset somewhat by the transient eddy moisture convergence and wetting. The changes in mean and transient moisture convergence amplify the corresponding climatological processes as shown in Fig. 2. The mean moisture convergence change is further divided into that due to circulation change (dynamic, DYN) and that due to specific humidity change (thermodynamic, TH) as shown in Eq. 5 (Fig. 7d,e). The dynamic term contributes negligibly to spring drying (Fig. 7d) and it is instead almost entirely caused by the thermodynamic contribution due to increases in specific humidity (Fig. 7e). The dominance of the thermodynamic term here may not be surprising. It might be thought that since this is a region of mean mass divergence, a warming-driven increase of moisture in the atmosphere would lead to more moisture divergence and hence drying. However, Figs. 7f and g illustrate that the thermodynamic change is almost entirely due to the climatological wind advecting the anomalous specific humidity gradient, while the climatological mean mass divergence of anomalous moisture is negligible. The dominance of the advection term seems to be consistent with the climatological moisture budget shown in Fig. 2. We next examine further how the moisture gradient changes in the future as the climate warms.

Figure 8a shows the vertical cross section of the spring zonally asymmetric specific humidity change between the end of the 21st Century and the current climate from CMIP5 MMM. There is an enhanced specific humidity gradient with reduced specific humidity to the west and enhanced humidity to the east of the domain. This causes anomalous dry advection by the climatological westerlies (Figs. 3c and 7f). To understand the causes of the change in specific humidity gradient we separate the humidity change using the Clausius-Clapeyron equation.

The specific humidity can be written approximately as: $q = rq_s$, where r is relative humidity (defined as the ratio of actual vapor pressure e and saturation vapor pressure e_s, r

= e/e_s) and q_s is the saturation specific humidity, which is only a function of temperature according to the Clausius-Clapeyron equation:

$$e_s = e_0 exp\left[\frac{L}{R_v}\left(\frac{1}{T_0} - \frac{1}{T}\right)\right],\ q_s \approx \frac{R_d}{R_v}\left(\frac{e_s}{p - e_s}\right) \qquad (6)$$

where e_0 represents the e_s value when T is equal to a reference temperature T_0, L is the latent heat of vaporization and R_d and R_v are the gas constants for dry air and water vapor, respectively, and p is the air pressure. Define the specific humidity change as

$$\Delta q = q_f - q_p = r_f q_s(T_f) - r_p q_s(T_p) = \Delta r q_s(T_p) + r_p \Delta q_s + \Delta r \Delta q_s \qquad (7)$$

where subscripts f and p represents future and past values and $\Delta = (\ \ )_f - (\ \ )_p$. If we ignore the nonlinear term in (7), then

$$\Delta q \approx \Delta r q_s(T_p) + r_p \Delta q_s \qquad (8)$$

where Δq_s can be written as:

$$\Delta q_s = q_s(T_p + \Delta T) - q_s(T_p)$$

Figure 8b shows the calculated Δq according to Eq. (8) with the zonal mean part removed (Δq*), which agrees well with the Δq* based on model outputs in Fig. 8a. If we assume relative humidity does not change in the future, an assumption, which has been shown to be a good approximation in both observations (Gaffen and Ross, 1999) and theoretically (Pierrehumbert et al., 2007), then equation 8 can be approximated by

$$\Delta q \approx r_p \Delta q_s = r_p\left[q_s(T_p + \Delta T) - q_s(T_p)\right] \qquad (9)$$

The resulting change in the zonally asymmetric specific humidity is shown in Fig. 8c, which reproduces well the actual model change but with somewhat larger amplitude. Thus, the change in air temperature (ΔT) with fixed relative humidity dominates the change in q.

The air temperature change in Eq. (9) can be further divided into zonal mean change and zonally asymmetric change in air temperature as follows:

$$\Delta q \approx r_p\left[q_s\left(T_p + \langle\Delta T\rangle + \Delta T^*\right) - q_s\left(T_p\right)\right] \quad (10)$$

where angle bracket represents the zonal mean value, and asterisk the zonally asymmetric component. It is clear from Fig. 8d that the zonally asymmetric q change above 700 hPa is largely explained by the zonal mean temperature change ($\langle\Delta T\rangle$). Figures 8e and f show the changes in zonally asymmetric q due to ΔT^* only (by setting $<\Delta T>$ to zero in Eq. 10) and relative humidity only (setting Δq_s to zero in Eq. 8), respectively. The contribution to the zonally asymmetric q change is relatively minor in both cases compared to that due to the zonal mean temperature change (Fig. 8c). Zonally uniform temperature change ($<\Delta T>$) leads to zonally asymmetric specific humidity change (Δq^*) because land is warmer than ocean in the spring and, hence, when adding a uniform temperature increase to both land and ocean, specific humidity increases more over land than ocean due to the nonlinear Clausius-Clapeyron relation (Eq. 6). It is, however, very interesting that the specific humidity change is dominated by the zonal mean temperature change, rather than the asymmetric warming of the land and ocean in the future, or changes in relative humidity (Byrne and O'Gorman, 2015).

To confirm the change in zonal mean temperature, which led to the enhanced q gradient, is indeed the dominant cause of the spring drying, we computed the corresponding change in vertically integrated mean moisture convergence ($\delta\left(\overline{-\frac{1}{g\rho_w}\nabla\cdot\int_0^{p_s}\bar{\bar{u}}\,\bar{q}dp}\right)$), due to each q change as shown in Fig. 8. The results are shown in Fig. 9 for the spring season. Consistent with Fig. 8, Figs. 9a and b are almost identical, indicating that the calculated specific humidity using the Clausius-Clapeyron equation reproduces well the CMIP5

MMM q. Both Figs. 9 a and b show drying in the SWUS and wetting in the east half of the country, and bear some similarities to the MMM P – E pattern in Fig. 5d. This pattern is largely reproduced when assuming constant relative humidity (c) and when only allowing the zonally symmetric temperature to change (d). In contrast, the contributions to this pattern due to change in the zonally asymmetric temperature (e) and only allowing relative humidity to change (f) are relatively small.

The enhanced q gradient is also seen in summer and fall (not shown). However, the climatological wind speed is weaker in those seasons than in spring and the enhanced dry zonal advection is also less explaining the maximum drying of the region in spring.

Zonal mean temperature changes under greenhouse warming is a relatively robust feature of the CMIP5 models, thus spring drying in SWUS is also very robust, as can be seen in Figs. 6 and 7. We find it interesting that the robust spring drying under global warming can be explained largely by thermodynamic processes through the zonal mean temperature changes, meaning that the change in atmospheric circulation plays little role in causing the drying. The dominance of thermodynamic processes may not be surprising but this advective mechanism is distinct from the well-known “dry get drier” mechanism. The “dry get drier” mechanism best applies over the oceans to regions of climatological mass and moisture divergence and negative P-E and largely explains the large scale drying over subtropical oceans (Held and Soden, 2006). Over land, there is mean moisture convergence, P-E is positive and a simple application of Held and Soden arguments implies wetting. However, drying over land can still occur due to thermodynamic processes and, in the case of the SWUS, it is enhanced advective drying that is the prime mechanism.

5. Summary

We explored the detailed mechanisms that caused the robust spring drying over SWUS under greenhouse warming as projected by the CMIP5 multimodel mean. While the conventional wisdom may be that the SWUS is located in a region of mean mass divergence, thus the increase of moisture in the atmosphere as a result of warming would lead to more moisture divergence, an application over land of the so-called "dry get drier" mechanism (Held and Soden, 2006), we find that is not the dominant mechanism in this case. In fact, even in the climatological sense, the mean mass divergence is not the dominant mechanism for the region being semi-arid in the first place. The spring and summer SWUS drying, on the other hand, is dominated by the zonal mean advection of drier air into the region due to the strong east-west humidity gradient. Intuitively, one would expect the westerlies to advect moist ocean air into the drier land region, thus causing wetting of the region. However, due to the land-ocean thermal contrasts and the topography of the region, land is warmer than ocean during the spring, summer and fall seasons allowing a maximum in specific humidity in the highland surface region and a specific humidity gradient with increasing moisture inland. In the greenhouse future, when a zonally uniform warming is added to the existing land-ocean thermal contrasts, the anomalous specific humidity gradient intensifies due to the nonlinearity of the Clausius-Clapeyron relationship. With the stronger climatological westerlies in the spring compared to summer and fall, the anomalous mean moisture advection due to the climatological flow advecting the anomalous specific humidity gradient reaches a maximum in the spring, causing robust spring drying in SWUS. The effect increases linearly from the near future

(2021-2040) to the end of the 21st Century, and shows extreme robustness across the CMIP5 models.

The mechanism here seems to be consistent with Byrne and O'Gorman (2015) in that the horizontal gradients of changes in temperature and relative humidity need to be taken into account to explain the P-E response to warming over land. However, we found that it is not the changes in temperature gradient, but rather the nonlinear response of the specific humidity gradient to the zonal mean warming superimposed on the zonally asymmetric land-ocean thermal contrasts, that dominates the spring drying in the Southwest United States. The contributions from both the change in zonally asymmetric temperature and change in relative humidity are relatively small.

There are important implications of the spring drying in the SWUS. Currently the peak drying season is in the summer months, while winter and early spring provide much needed supply of water and water storage to the region. Since CMIP5 tends to have a wet bias in P-E (Fig. 2), we can crudely correct for this by subtracting from the model future P-E for each month the constant annual mean bias value of 0.54 mm/day. The resulting seasonal cycle of P – E for each of the future period is shown in Fig. 10. When the seasonal cycle shifts toward a drier spring, there is much reduced positive P-E in March and substantially increased negative P-E in April, May and June (Fig. 10). The total reduction of surface water of the entire season from March to June will prolong and intensify the dry season. This will adversely impact the spring growing season, potentially increase fire risk, degrade pasturelands, rangelands, and crops and lower spring and summer streamflow. Although spring drying is dominant and has been the focus here, there is also substantial drying in the fall season, as can be seen in Figs. 6 and 10. Coupled with early melt of snow cover due to warming, a shortened winter wet season could substantially reduce the SWUS water supply and storage in the future.

Acknowledgments. This study was supported by the National Science Foundation EaSM2 grant AGS 12-43204 and National Oceanic and Atmospheric Administration grant NA14OAR4310223. We would also like to thank the two anonymous reviewers for helpful suggestions that led to many improvements.

References

Boos, W. R., 2012: Thermodynamic Scaling of the Hydrological Cycle of the Last Glacial Maximum. *J. Climate*, **25**, 992-1006.

Byrne, M. P. and P. A. O'Gorman, 2015: The Response of Precipitation Minus Evapotranspiration to Climate Warming: Why the "Wet-Get-Wetter, Dry-Get-Drier" Scaling Does Not Hold over Land. J. Climate, 28, 8078-8092.

Cook, B. I., J. E. Smerdon, R. Seager, and S. Coats, 2014: Global warming and 21st century drying, *Clim. Dyn*., **43**(9–10), 2607–2627, doi:10.1007/s00382-014-2075-y.

Cook, B. I., T. R. Ault, and J. E. Smerdon, 2015: Unprecedented 21st century drought risk in the American Southwest and Central Plains, *Sci. Adv.*, **1**(1), e1400082, doi:10.1126/sciadv.1400082.

Dee et al., 2011: The ERA-Interim reanalysis: configuration and performance of the data assimilation system. *Q. J. R. Meteorol. Soc.*, **137**, 553–597.

Diffenbaugh, N. S., D. L. Swain, and D. Touma, 2015: Anthropogenic warming has increased drought risk in California, *Proc. Natl. Acad. Sci. U.S.A*., **112**(13), 3931–3936, doi:10.1073/pnas.1422385112.

Gaffen, D. J., and R. J. Ross, 1999: Climatology and trends of U.S. surface humidity and temperature. J. Climate, 12, 811–828, doi:10.1175/1520 0442.

Gao, Y., L. R. Leung, J. Lu, Y. Liu, M. Huang, and Y. Qian (2014), Robust spring drying in the southwestern U.S. and seasonal migration of wet/dry patterns in a warmer climate, *Geophys. Res. Lett*., **41**, 1745–1751, doi:10.1002/2014GL059562.

Held, I. M. & Soden, B. J., 2006: Robust responses of the hydrological cycle to global warming. *J. Climate*. **19**, 5686–5699.

Jiang, X., N.-C. Lau, I. M. Held, and J. J. Ploshay, 2007: Mechanisms of the Great Plains Low-Level Jet as Simulated in an AGCM. *J. Atmos. Sci.*, **64**, 532-547.

Luce, C. H., V. Lopez-Burgos, and Z. Holden, 2014: Sensitivity of snowpack storage to precipitation and temperature using spatial and temporal analog models. *Water Resources Research*, **50**, 9447–9462.

Mote, P. W., 2006: Climate-Driven Variability and Trends in Mountain Snowpack in Western North America. *J. Climate*, **1**9, 6209-6220.

Parish T. R., and L. D. Oolman, 2010: On the Role of Sloping Terrain in the Forcing of the Great Plains Low-Level Jet. *J. Atmos. Sci.*, **67**, 2690-2699.

Pierce, D. W., Barnett, T. P., Hidalgo, H. G., et al., 2008: Attribution of declining western U.S. snowpack to human effects. Journal of Climate, 21, 6425–6444.

Pierrehumbert, R., H. Brogniez, and R. Roca, 2007: On the relative humidity of the atmosphere. The Global Circulation of the Atmosphere, T. Schneider and A. H. Sobel, Eds., Princeton University Press, 143–185.

Prein, A. F., G. J. Holland, R. M. Rasmussen, M. P. Clark, and M. R. Tye, 2016: Running dry: The U.S. Southwest's drift into a drier climate state, *Geophys. Res. Lett*., **43**, 1272–1279, doi:10.1002/2015GL066727.

Scheff, J., and D. M. Frierson, 2012: Robust future precipitation declines in CMIP5 largely reflect the poleward expansion of model subtropical dry zones, *Geophys. Res. Lett.*, **39**, L18704, doi:10.1029/2012GL052910.

Seager, R. and N. Henderson, 2013: Diagnostic Computation of Moisture Budgets in the ERA-Interim Reanalysis with Reference to Analysis of CMIP-Archived Atmospheric Model Data. *J. Climate*, **26**, 7876-7901.

Seager, R., D. Neelin, I. Simpson, H. Liu, N. Henderson, T. Shaw,Y. Kushnir, M. Ting, 2014: Dynamical and thermodynamical causes of large-scale changes in the hydrological cycle over North America in response to global warming. *J. Climate*, **27**, 7921-7948, doi: http://dx.doi.org/10.1175/JCLI-D-14-00153.1.

Seager, R., M. Hoerling, S. Schubert, H. L. Wang, B. Lyon, A. Kumar, J. Nakamura and N. Henderson, 2015: Causes of the 2011-14 California Drought. *Journal of Climate*, 28(18): 6997-7024, DOI: 10.1175/JCLI-D-14-00860.1.

Seager, R., M. Ting, I. Held, Y. Kushnir, J. Lu, G. Vecchi, H.-P. Huang, Nili Harnik, A. Leetmaa, N.-C. Lau, C. Li, J. Velez, N. Naik, 2007: Model Projections of an Imminent Transition to a More Arid Climate in Southwestern North America. *Science*, DOI: 10.1126/science.1139601.

Seager, R., M. Ting, C. Li, N. Naik, B. Cook, J. Nakamura, and H. Liu, 2013: Projections of declining surface water availability for the southwestern U.S. *Nature Climate Change*, 678 3, 482-486.

Seager, R., and G. A. Vecchi, 2010: Greenhouse warming and the 21st century hydroclimate of southwestern North America. *Proc Natl Acad Sci USA*, **107**, 21277–21282.

Taylor, K. E., R. J. Stouffer, and G. A. Meehl, 2012: AN Overview of CMIP5 and the experiment design. *Bull. Amer. Meteor. Soc*., DOI:10.1175/BAMS-D-11-00094.1.

Ting, M. and H. Wang, 2006: The Role of the Rockies in the Maintenance of US Summer Precipitation and Low-Level Jet. *J. Atmos. Sci*., **63**, 1056-1068.

List of Figures

FIG. 1. Precipitation minus evaporation (P – E) from ERA-Interim Reanalysis (left) and CMIP5 MMM (right) averaged for the period 1979-2005 for DJF (a, b), MAM (c, d), JJA (e, f), and SON (g, h). Units are in mm/day and contour interval is 1 mm/day.

FIG. 2. The climatological mean (1979-2005) seasonal cycle of the moisture budget terms averaged over the Southwest United States (the outlined region in Fig. 1) for ERA-Interim Reanalysis (left) and CMIP5 MMM (right). (a) and (b): precipitation minus evaporation, (c) and (d): column averaged mean flow moisture convergence (MC), (e) and (f): column averaged sub-monthly transient eddy MC, (g) and (h): column averaged MC due to mean moisture advection, (i) and (j): column averaged MC due to mean flow mass divergence, and (k) and (l): the surface boundary term due to surface pressure gradient.

FIG. 3. Longitude-pressure cross sections of the climatological mean (1979 – 2005) zonally asymmetric temperature (black contours), zonally asymmetric specific humidity (green contours) and total zonal wind vectors averaged from 32N - 45N using ERA-Interim Reanalysis (left) and CMIP5 MMM (right) for DJF (a, b), MAM (c, d), JJA (e, f), and SON (g, h). Contour intervals are 0.5oC for temperature and 0.25 g/kg for specific humidity and negative values are dashed.

FIG. 4. Vertically integrated mean moisture transport (arrows) and 850 hPa specific humidity (shading) for ERA Interim (left) and CMIP5 MMM (right) for the four seasons averaged for the period 1979-2005. The unit is g/kg for specific humidity and kg/m^2 m/s for moisture fluxes. Vector scale is shown at the lower left.

FIG. 5. The changes in P – E (a), mean moisture convergence (b), and transient moisture convergence (c) based on CMIP5 MMM's RCP8.5 future scenario simulations for the

period 2021-2040, 2041-2060, 2061-2080, and 2081-2099 with respect to the historical simulation averaged from 1979-2005, averaged over the Southwest United States land region from 125W-103W and 25N to 45N.

FIG. 6. Changes in P – E for March, April and May seasonal average based on CMIP5 MMM RCP8.5 scenario simulations for 2021-2040 (a), 2041-2060 (b), 2061-2080 (c), and 2081-2099 (d), with respect to the 1979-2005 historical simulation.

FIG. 7. Changes in the various moisture budget terms for March, April and May seasonal average based on CMIP5 MMM RCP8.5 scenario simulations for the four future periods with respect to the 1979-2005 historical simulation for (a) P – E, (b) Mean moisture convergence (MC), (c) transient MC, (d) mean MC due to changes in atmospheric circulation only (DYN), (e) mean MC due to changes in specific humidity only (TH), (f) the part in (e) due to climatological mean flow advecting anomalous specific humidity gradient, and (g) the part in (e) due to climatological mass divergence of the anomalous specific humidity.

FIG. 8. Longitude-vertical cross sections of the zonally asymmetric specific humidity change (2075-2099 minus 1979-2005) for (a): CMIP5 MMM, (b): calculated based on Clausius-Clapeyron equation and given the relative humidity and temperature changes, (c): same as (b), but with fixed relative humidity and only allow the temperature to change, (d): same as in (c) but only allow the zonal mean temperature to change, (e): same as in (c) but only allow the zonally asymmetric temperature to change, and (f): same as in (b) but only allow the relative humidity to change. Contour interval is 0.05 g/kg and negative contours are dashed.

Figure 9. Changes in vertically integrated mean moisture convergence between averages for the period (2075 - 2099) and (1979 - 2005) calculated using (a): CMIP5 MMM wind, specific humidity and surface pressure, (b) same as (a) except using the specific humidity calculated from Clausius-Clapeyron equation given MMM relative humidity and temperature changes, (c): same as (b), but with fixed relative humidity and only allow the temperature to change, (d): same as in (c) but only allow the zonal mean temperature to change, (e): same as in (c) but only allow the zonally asymmetric temperature to change, and (f): same as in (b) but only allow the relative humidity to change. Contour interval is 0.4 mm/day and negative contours are dashed.

FIG. 10. Bias-corrected (subtracting a 0.54 mm/day wet bias from each month to correct the annual mean P-E difference between models and ERA-I Reanalysis) seasonal cycle of P – E for five different periods as simulated by the CMIP5 MMM for the US Southwest domain (box shown in Fig. 5). Future simulations are the RCP8.5 scenario, and past simulations use CMIP5 historical forcing.

TABLE 1. CMIP5 models used in this study, including their originating institutions, horizontal and vertical resolutions, and ensemble sizes.

Institute	Model	Resolution (lon x lat), level	Ensemble size	
			20thC	rcp85
Beijing Climate Center (BCC)	1. bcc-csm1-1	T42, L26	1	1
	2. bcc-csm1-1-m	T106, L26	1	1
College of Global Change and Earth System Science, Beijing Normal University (BNU)	3. BNU-ESM	T42, L26	1	1
Canadian Centre for Climate Modeling and Analysis (CC-Cma)	4. CanESM2	T63 (1.875°x1.875°), L35	1	1
National Center for Atmospheric Research (NCAR)	5. CCSM4	288x200 (1.25°x0.9°), L26	1	1
Centro Euro-Mediterraneo per I Cambiamenti Climatici (CMCC)	6. CMCC-CM	T159, L31	1	1
Centre National de Recherches Meteorologiques / Centre Europeen de Recherche et Formation Avancees en Calcul Scientifique (CNRM-CERFACS)	7. CNRM-CM5	T127(1.4°x1.4°), L31	1	1
Commonwealth Scientific and Industrial Research Organisation in collaboration with the Queensland Climate Change Centre of Excellence (CSIRO-QCCCE)	8. CSIRO-Mk3-6-0	T63(1.875°x1.875°), L18	1	1
Institute of Atmospheric Physics, Chinese Academy of Sciences and Tsinghua University (LASG-CESS)	9. FGOALS-g2	128x60, L26	2	1
Geophysical Fluid Dynamics Laboratory (NOAA GFDL)	10. GFDL-CM3	C48 (2.5°x2.0°), L48	5	1
	11. GFDL-ESM2G	144x90 (2.5°x2.0°), L24	1	1
	12. GFDL-ESM2M	144x90 (2.5°x2.0°), L24	1	1
NASA Goddard Institute for Space Studies (NASA GISS)	13. GISS-E2-H	2.5°x2°, L40	1	1
	14. GISS-E2-R	2.5°x2°, L40	1	1
Institut Pierre-Simon Laplace (IPSL)	15. IPSL-CM5A-LR	3.75°x1.875°, L39	6	3
	16. IPSL-CM5A-MR	2.5°x1.25°, L39	2	1
	17. IPSL-CM5B-LR	96x96 (3.75°x1.875°), L39	1	1
Atmosphere and Ocean Research Institute (The University of Tokyo), National Institute for Environmental Studies, and Japan Agency for Marine-Earth Science and Technology (AORI/NIES/JAMSTEC)	18. MIROC5	T85, L40	5	1
	19. MIROC-ESM	T42, L80	3	1
	20. MIROC-ESM-CHEM	T42, L80	1	1
Meteorological Research Institute (MRI)	21. MRI-CGCM3	TL159 (1.125°x1.125°), L48	1	1
Norwegian Climate Centre (NCC)	22. NorESM1-M	144x96 (2.5°x1.875°), L26	3	1

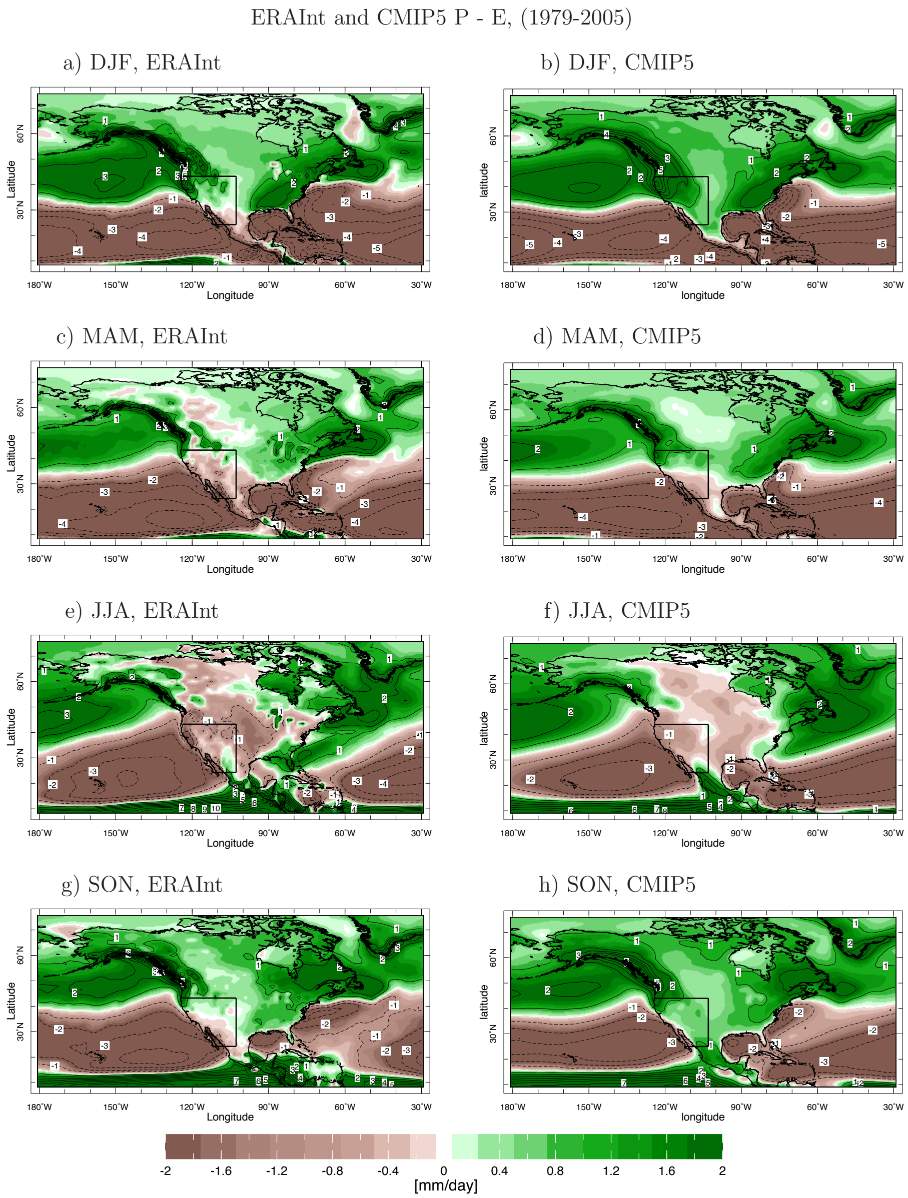

FIG. 1. Precipitation minus evaporation (P – E) from ERA-Interim Reanalysis (left) and CMIP5 MMM (right) averaged for the period 1979-2005 for DJF (a, b), MAM (c, d), JJA (e, f), and SON (g, h). Units are in mm/day and contour interval is 1 mm/day.

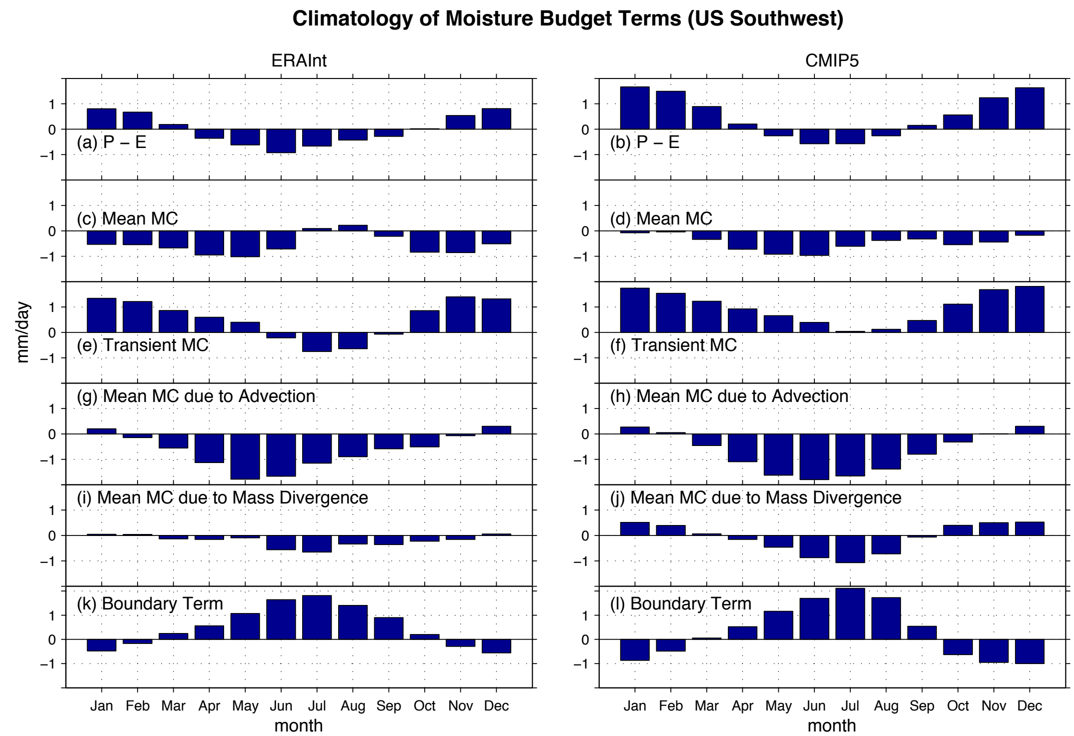

FIG. 2. The climatological mean (1979-2005) seasonal cycle of the moisture budget terms averaged over the Southwest United States (the outlined region in Fig. 1) for ERA-Interim Reanalysis (left) and CMIP5 MMM (right). (a) and (b): precipitation minus evaporation, (c) and (d): column averaged mean flow moisture convergence (MC), (e) and (f): column averaged sub-monthly transient eddy MC, (g) and (h): column averaged MC due to mean moisture advection, (i) and (j): column averaged MC due to mean flow mass divergence, and (k) and (l): the surface boundary term due to surface pressure gradient.

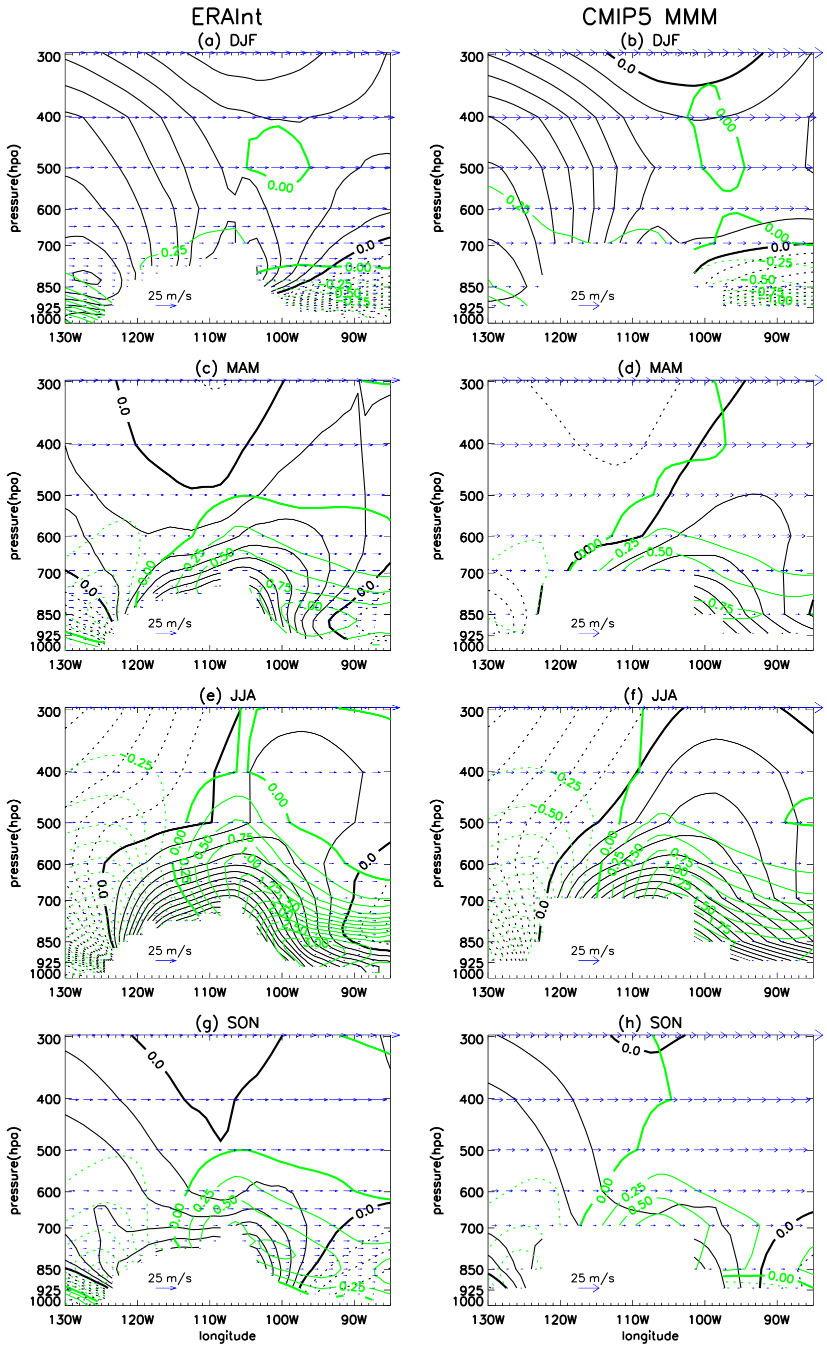

FIG. 3. Longitude-pressure cross sections of the climatological mean (1979 – 2005) zonally asymmetric temperature (black contours), zonally asymmetric specific humidity (green contours) and total zonal wind vectors averaged from 32N - 45N using ERA-Interim Reanalysis (left) and CMIP5 MMM (right) for DJF (a, b), MAM (c, d), JJA (e, f), and SON (g, h). Contour intervals are 0.5^{o}C for temperature and 0.25 g/kg for specific humidity and negative values are dashed.

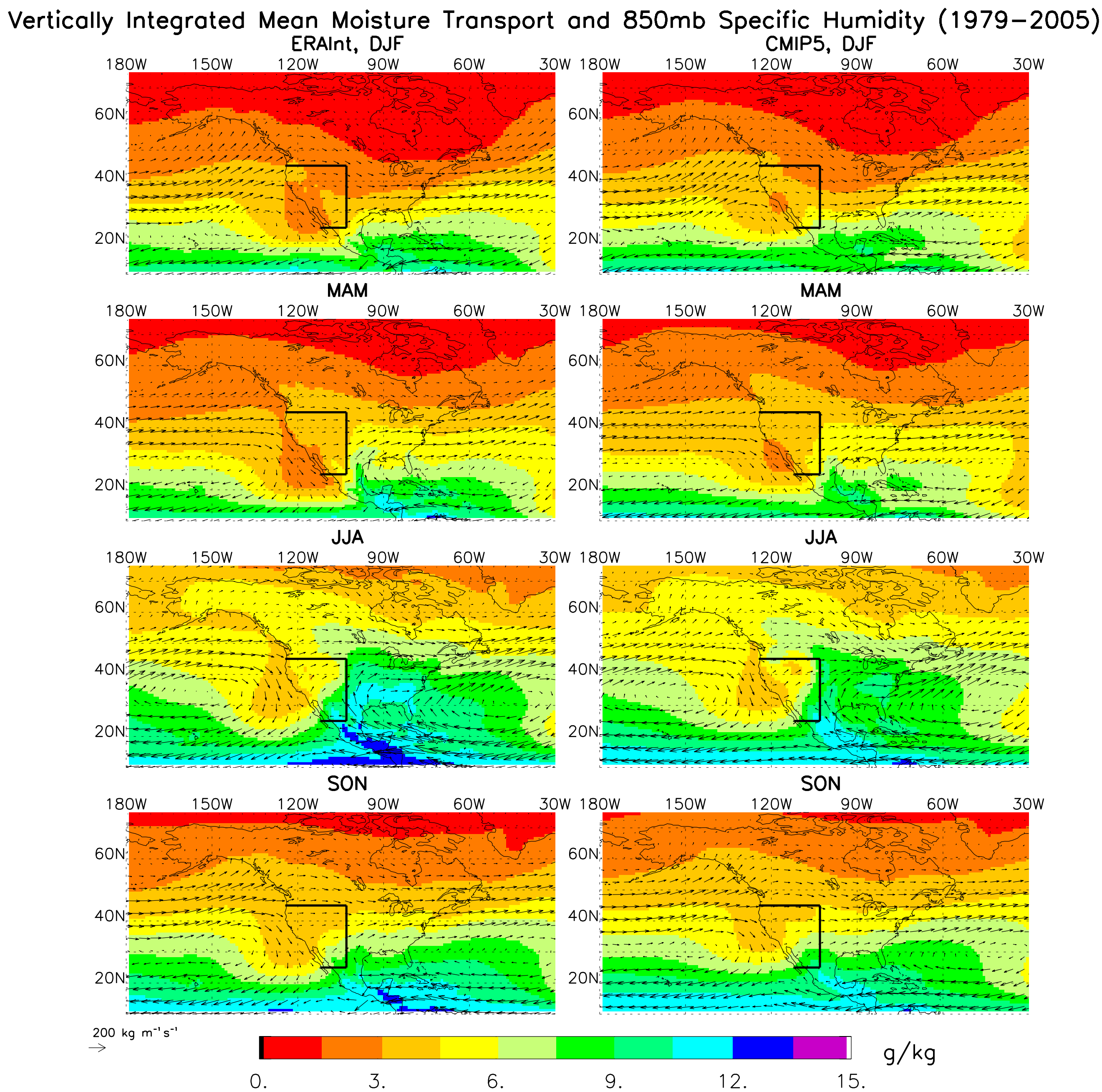

Fig. 4. Vertically integrated mean moisture transport (arrows) and 850 hPa specific humidity (shading) for ERA Interim (left) and CMIP5 MMM (right) for the four seasons averaged for the period 1979-2005. The unit is g/kg for specific humidity and kg/m^2 m/s for moisture fluxes. Vector scale is shown at the lower left.

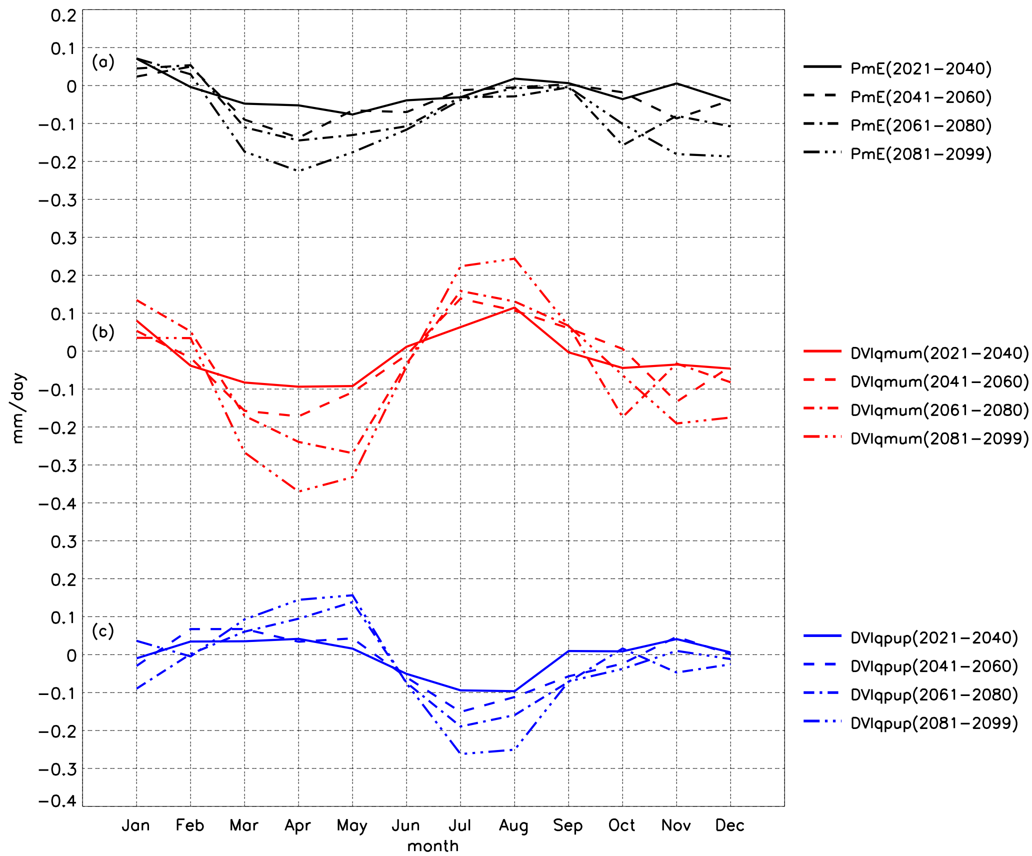

FIG. 5. The changes in P – E (a), mean moisture convergence (b), and transient moisture convergence (c) based on CMIP5 MMM's RCP8.5 future scenario simulations for the period 2021-2040, 2041-2060, 2061-2080, and 2081-2099 with respect to the historical simulation averaged from 1979-2005, averaged over the Southwest United States land region from 125W-103W and 25N to 45N.

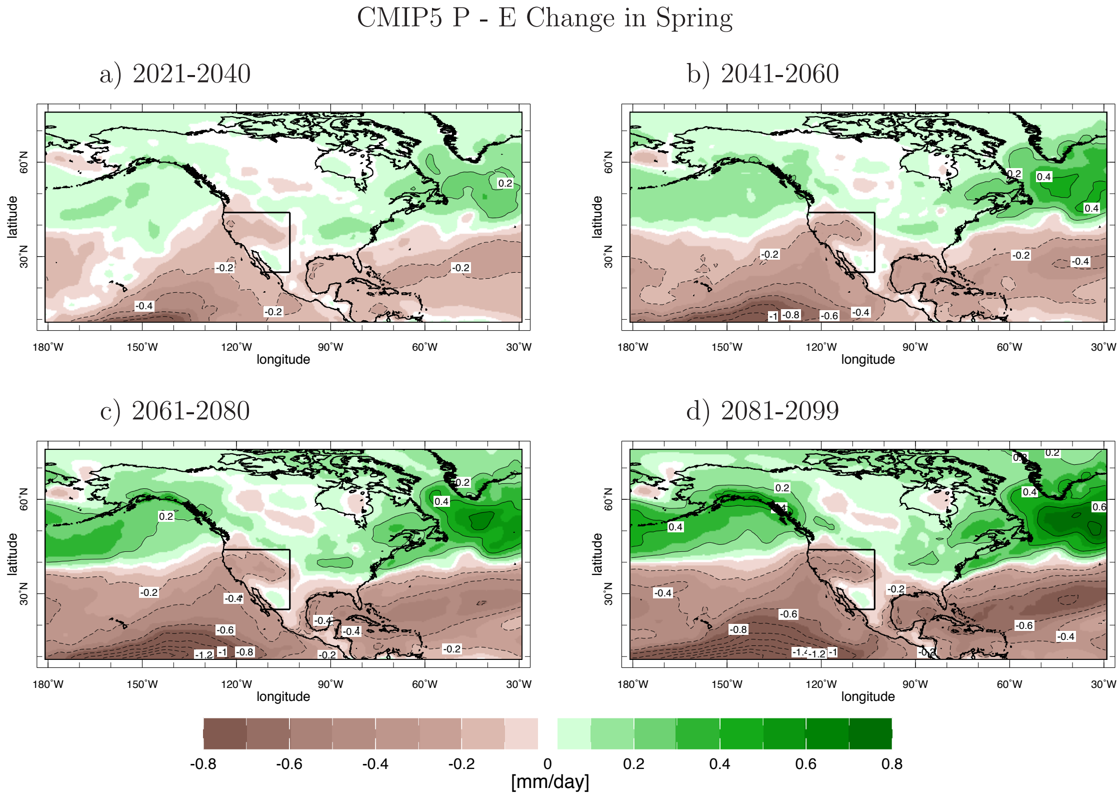

FIG. 6. Changes in P – E for March, April and May seasonal average based on CMIP5 MMM RCP8.5 scenario simulations for 2021-2040 (a), 2041-2060 (b), 2061-2080 (c), and 2081-2099 (d), with respect to the 1979-2005 historical simulation.

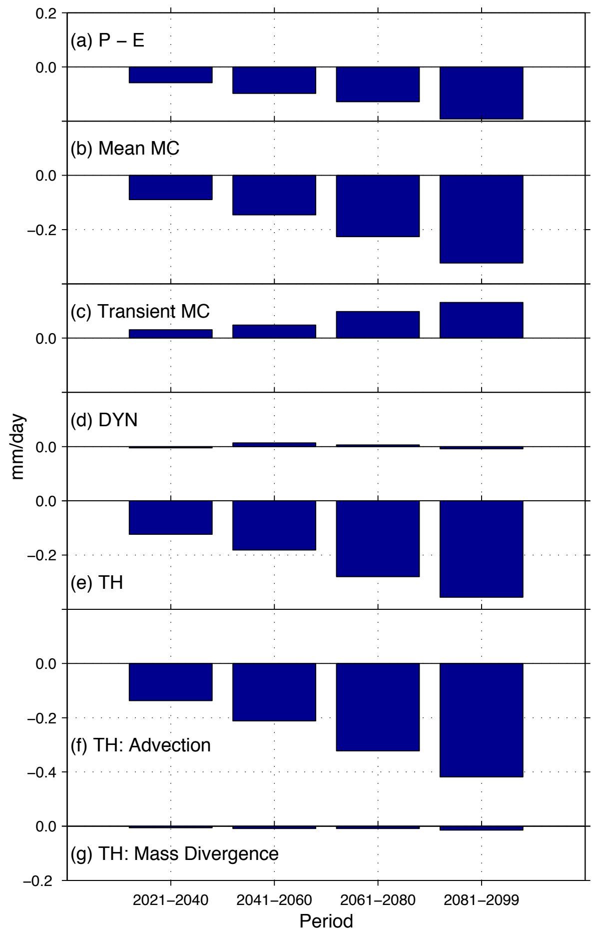

FIG. 7. Changes in the various moisture budget terms for March, April and May seasonal average based on CMIP5 MMM RCP8.5 scenario simulations for the four future periods with respect to the 1979-2005 historical simulation for (a) P – E, (b) Mean moisture convergence (MC), (c) transient MC, (d) mean MC due to changes in atmospheric circulation only (DYN), (e) mean MC due to changes in specific humidity only (TH), (f) the part in (e) due to climatological mean flow advecting anomalous specific humidity gradient, and (g) the part in (e) due to climatological mass divergence of the anomalous specific humidity.

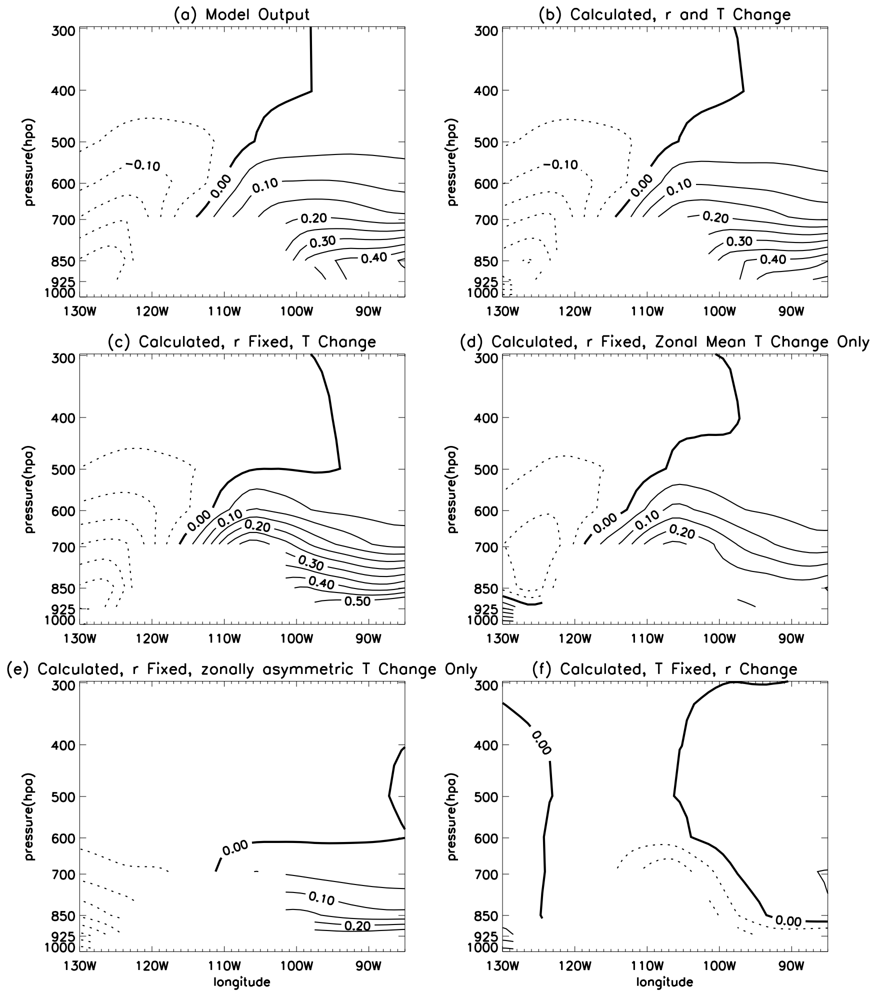

FIG. 8. Longitude-vertical cross sections of the zonally asymmetric specific humidity change (2075-2099 minus 1979-2005) for (a): CMIP5 MMM, (b): calculated based on Clausius-Clapeyron equation and given the relative humidity and temperature changes, (c): same as (b), but with fixed relative humidity and only allow the temperature to change, (d): same as in (c) but only allow the zonal mean temperature to change, (e): same as in (c) but only allow the zonally asymmetric temperature to change, and (f): same as in (b) but only allow the relative humidity to change. Contour interval is 0.05 g/kg and negative contours are dashed.

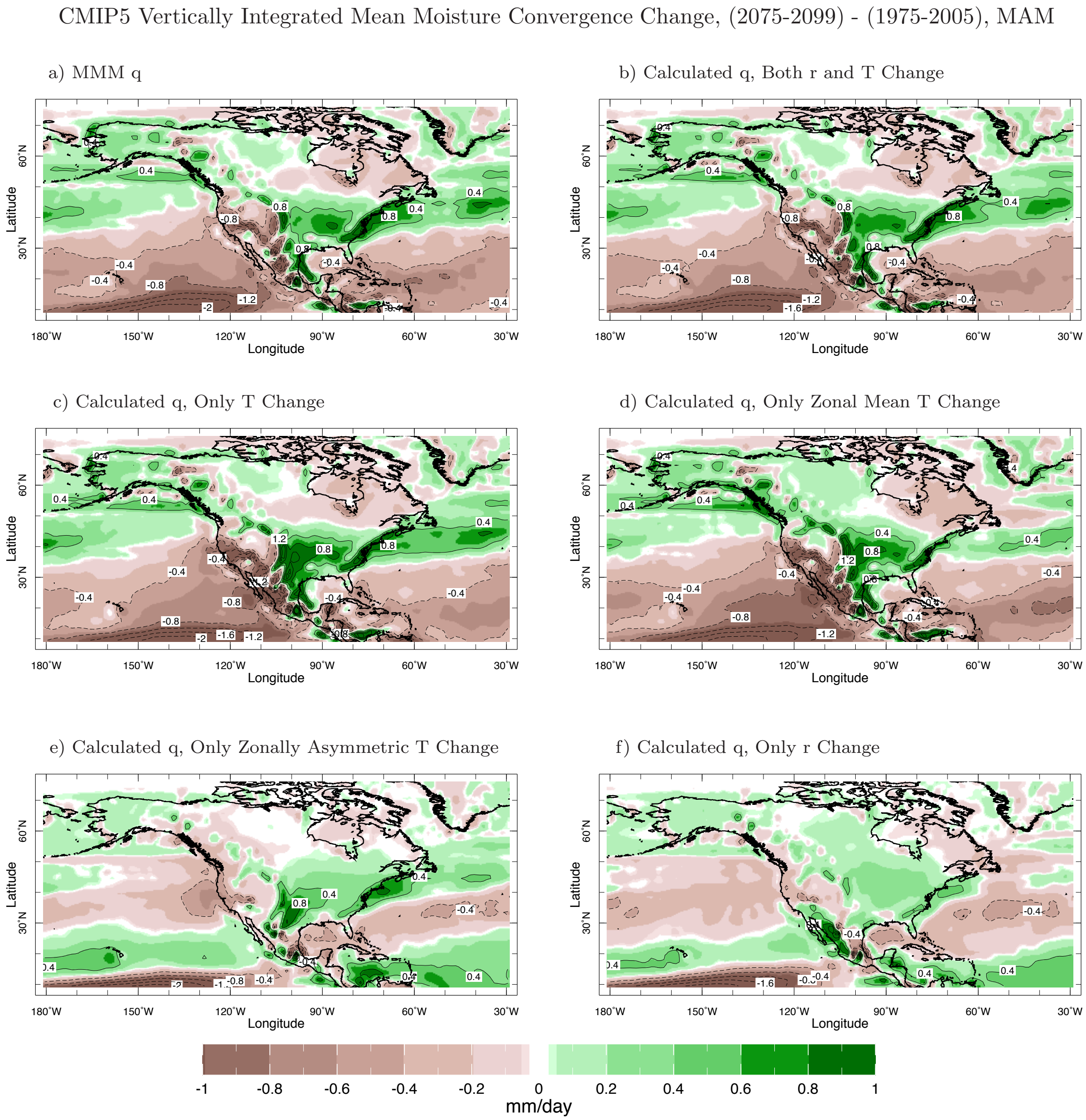

Figure 9. Changes in vertically integrated mean moisture convergence between averages for the period (2075 - 2099) and (1979 - 2005) calculated using (a): CMIP5 MMM wind, specific humidity and surface pressure, (b) same as (a) except using the specific humidity calculated from Clausius-Clapeyron equation given MMM relative humidity and temperature changes, (c): same as (b), but with fixed relative humidity and only allow the temperature to change, (d): same as in (c) but only allow the zonal mean temperature to change, (e): same as in (c) but only allow the zonally asymmetric temperature to change, and (f): same as in (b) but only allow the relative humidity to change. Contour interval is 0.4 mm/day and negative contours are dashed.

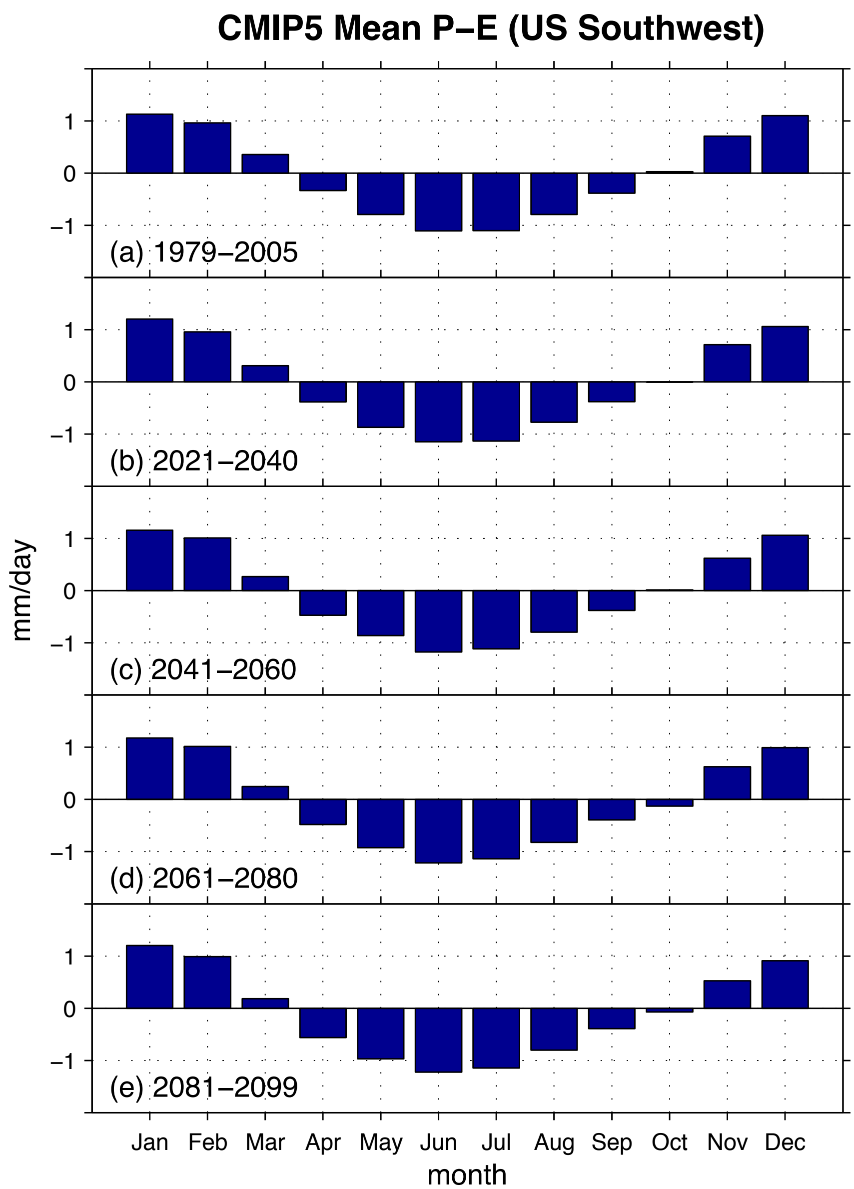

FIG. 10. Bias-corrected (subtracting a 0.54 mm/day wet bias from each month to correct the annual mean P-E difference between models and ERA-I Reanalysis) seasonal cycle of P – E for five different periods as simulated by the CMIP5 MMM for the US Southwest domain (box shown in Fig. 5). Future simulations are the RCP8.5 scenario, and past simulations use CMIP5 historical forcing.